Deformation mechanisms in submicron Be wires

Frédéric Mompiou[a)] and Marc Legros
Centre d'Elaboration de Matériaux et d'Etudes Structurales, UPR CNRS 8011 and Université de Toulouse, Toulouse 31055, France

Sylvie Lartigue-Korinek
Institut de Chimie des Matériaux Paris Est, UMR CNRS 7182, Thiais 94320, France

(Received 4 May 2017; accepted 20 July 2017)

Plastic deformation of small metallic single crystals has focused a lot of attention because of their enhanced or specific mechanical properties. Here, submicron beryllium wires, obtained from selective etching of an Al/Be eutectic alloy, were deformed in tension in situ using a transmission electron microscope. Our observations indicate that wires oriented parallel to their $\langle c \rangle$ axis and containing almost no dislocations present a fragile-like behavior associated to a high stress level. $\{10\bar{1}2\}$ $\langle 1011 \rangle$ twins were also frequently observed near fractured wires, indicating that this deformation mode is important in small-scale Be. In a twinned area, a locally ductile behavior was observed due to the favorable orientation for prismatic slip. We also stress out the importance of a remaining outer layer, made of Al oxide, in the plastic deformation. On the basis of finite element modeling, we show that the deformation of the wire may involve dislocations moving along the wire axis, in or close to the Be/Al oxide interface, in agreement with in situ observations. Thus, even in naturally oxidized wires, the outer layer is supposed to play an important role in the deformation, not only in modifying a stress/strain field but also presumably in facilitating diffusional processes, such as dislocation climb or dislocation nucleation.

I. INTRODUCTION

The development, about 10 years ago, of FIB-machining and nanomechanical testing of submicron single crystals raised some eyebrows in the scientific community for revealing a size-dependent strength without apparent confinement. Subsequently, a large amount of data on the mechanical properties of micron- and submicron sized objects has been collected. Most of these earlier experiments focused on fcc crystals and reported a clear power-law-type increase of the yield stress with decreasing crystal size.[1,2] Later on, it appeared that this size effect was strongly sensitive to the initial microstructure, either because of the creation of FIB-related defects near the surface or because of the initial presence of dislocations.[3–5] These power-law-type size effects have been recently rationalized in terms of dislocation line tension competing with Peierls-type stresses[6] or using statistics on preexisting defects.[7] Again, this highlighted the importance of the initial dislocation microstructure. In hcp metals, apart from the existence of thermally activated mechanisms, plastic anisotropy introduces another degree of complexity that needs to be carefully discussed when analyzing the results.[8] For these reasons, the existence of a size effect in small wires and pillars is more controversial in such metals.[9,10] As for cubic crystals, the size effect is indeed both orientation and microstructure dependent.[11,12] In addition to dislocation slip, mechanical twinning in small specimens is expected to strongly impact their deformation behavior due to the complete reorientation of the different slip systems in the whole sample.[13] While Mg and Ti were not extensively studied in submicron specimens, even less attention was paid to other hcp metals.

Beryllium deforms by dislocation slip on the basal and prismatic planes.[14,15] Prismatic glide exhibits a strong anomalous increase of the yield stress with temperature close to room temperature, which can be ascribed to strong friction stresses.[16,17] In addition to dislocation slip, $\{10\bar{1}2\}$ twinning is also frequently activated. In a previous work, we have shown that a twin boundary can propagate under stress by the nucleation of twinning dislocations presumably from the surface.[18]

In the present article, our aim is to gain a deep understanding of the elementary mechanisms of plastic deformation at play in Be wires with the knowledge of the initial microstructure. Thus, we report in situ and postmortem transmission electron microscope (TEM) observations of submicron Be wires deformed in tension and fractured. After presenting our original experimental approach and set-up, we will give examples of typical deformation mechanisms including fracture-like deformation, twinning and dislocation slip. We will also stress out

Contributing Editor: Mathias Göken
a)Address all correspondence to this author.
e-mail: mompiou@cemes.fr
DOI: 10.1557/jmr.2017.327

that the oxide layer surrounding the wires plays a significant role in the accommodation mechanisms and presumably in the ability of the wires to locally generate nonuniform 3D stresses, themselves able to activate dislocation and twins.

II. EXPERIMENTAL

A directionally solidified Al–2.4 at.% Be eutectic alloy has been cut by electrodischarging machining parallel to the wire length. 3 by 1 mm samples were then mechanically polished and etched by a Struers A2 electrolytic solution at −10 °C. The fast etching of the aluminum matrix releases the Be wires in a circular etched region of 450 μm, corresponding to the diaphragm of the Struers electropolisher. The as-created TEM hole therefore contains several tens of wires of approximately the same diameter. Although bundles of superimposing wires are usually observed, isolated ones can be found principally in areas close to the TEM hole ridge [Fig. 1(a)]. Most of the wires have only one end attached to the rest of the matrix, but some are linked to both ends and can therefore be stretched. The wires were deformed by applying a uniaxial displacement on the sample glued on a copper grid.[18] In situ observations were performed on a JEOL2010 TEM (JEOL Ltd., Tokyo, Japan) operated at 200 kV. Video sequences were recorded on a hard drive/DVD writer using a MEGAVIEW III camera (Olympus Soft Imaging Solutions GmbH, Münster, Germany) at 22–25 fps. Chemical analysis of the wires was performed on a Philips CM20 FEG (Philips, Amsterdam, the Netherlands) operated at 200 kV and equipped with an Energy Dispersive Spectrometer SDD from Bruker (Bruker Corporation, Billerica, Massachusetts). Finally, the Finite Element Method was used to simulate stress distribution around a partially etched Be wire using the COMSOL Multiphysics software (COMSOL, Stockholm, Sweden).

III. RESULTS

Most of the wires in the hole are several tens of μm long. End-on observation of broken wires by SEM shows that the wires have a circular cross section [Fig. 1(a)]. The majority of the wires have a diameter of approximately 400 nm that is constant over the whole wire length, but wires with smaller diameters around 250 nm and some with a diameter constriction are also observed. Attached wires are usually straight and TEM observations reveal that most of them contain no dislocation. Wires that are detached at one end can be bent or cracked, and a high dislocation density is usually observed in the bent areas. Few $\{10\bar{1}2\}$ twins can also be observed. Scanning Transmission Electron Microscopy Energy Dispersive Spectroscopy performed on an individual wire reveals the presence of a thin oxide layer, presumably Al_2O_3 [Fig. 1(b)] at the wire surface. This layer is supposed to arise from an incomplete etching of the Al matrix close to the wire that eventually oxidized during or after etching. As explained below, a small layer containing Al still remains close to the surface of the wires. A line scan across the wire [Fig. 1(b)] clearly indicates the presence of Al and O elements at the periphery of the Be wire (see the wire in the inset with the chemical map). The oxide layer that contains either some Al oxide (Al_2O_3) or a mixture of Al and oxide (Al/Al_2O_3) is thus estimated to be around 15–20 nm. Three deformation mechanisms that may or may not be influenced by this remaining thin oxide have been identified in these wires and are described below.

A. Fragile-like fracture

Figure 2 illustrates a typical fracture-like behavior that occurred during an in situ straining experiment. Upon straining, a 250 nm wire broke abruptly [Figs. 2(a)–2(b), and video 1 in the Supplementary Material). Because of the accumulated elastic strain during the loading, the wire sudden failure has led to the back motion of the two parts of the broken wire over a few microns [Fig. 2(c)]. This fracture is however not comparable to what is observed in ceramics or semiconductors at low temperature as one end of the wire in the crack area clearly shows a high density of defects not present prior to deformation. It is therefore likely that a localized plastic event (nucleation

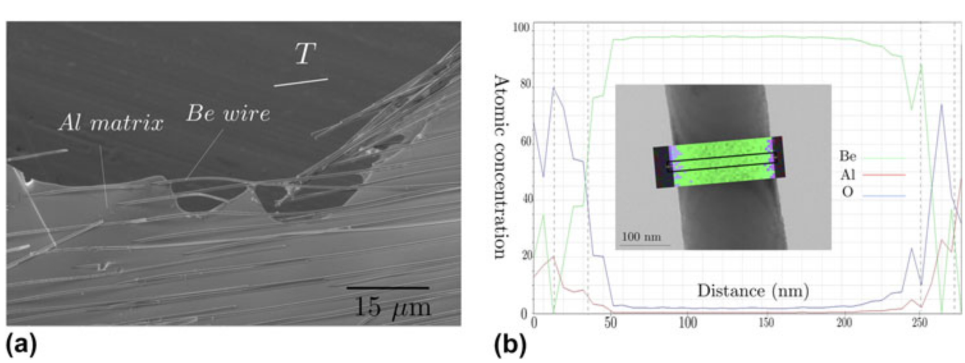

FIG. 1. (a) is a SEM image of a selectively etched Al/Be eutectic containing freestanding electron transparent Be wires surrounded by an Al matrix. (b) Atomic concentration of Be, Al and O elements along the line profile shown in the inset across a wire. The presence of an Al oxide at the wire surface is revealed.

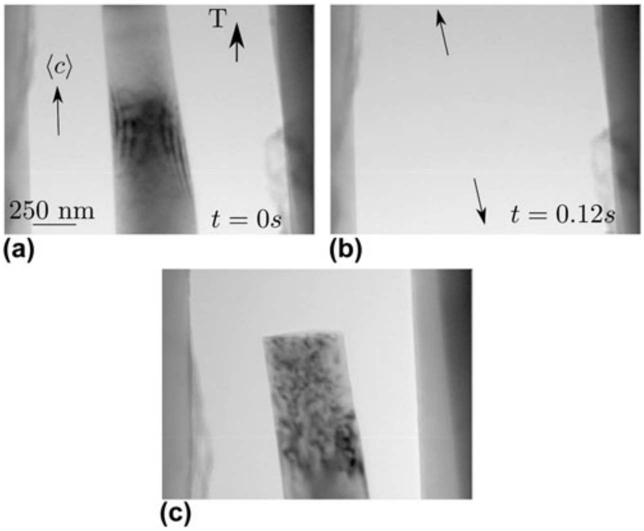

FIG. 2. Abrupt fracture-like failure observed upon straining in a 250 nm diameter, dislocation free wire.

followed by rapid multiplication of dislocations) occurred in a small volume [a wire length of about 550 μm—lower end of the wire, Fig. 2(c)] leading to an abrupt failure of the wire. Such a nucleation and multiplication event is likely to be too fast to be captured at the video rate of the camera (25 fps). A similar phenomenon is also observed in defect free Al wires.[4]

B. Twin migration

Smoother and more extended plastic deformation can however be observed associated to the migration of a $(01\bar{1}2)$ $[01\bar{1}\bar{1}]$ twin boundary as shown in Fig. 3. Twin migration over a distance of 4 μm has been observed after strain increments. The twin speed, reaching up to 12 nm/s, gradually decreases until the stress relaxed under a critical value below which the twin remained immobile.[19] In this case, several wires are grouped in a bundle, which produces several gray levels when the electron beam goes through superimposed wires. The sketch in Fig. 3(a) shows a possible stacking configuration of the 4 wires in which only the twinned one (green) is monitored during deformation. In the subsequent images, the wire of interest is delimited in green [and the others are delimited with dashed lined whose colors are related to Fig. 3(a)]. Figures 3(b) and 3(c) show two snapshots of the twin positions taken 21 s apart (for the corresponding video see the Supplementary Material). The twin motion appears continuous at a velocity of few nm/s. The migration distance $d_\perp$ can be clearly visualized by making an image subtraction (b) − (c) [Fig. 3(d)] with a fiducial marker X set as a fixed point. Then, an unchanged area appears uniformly gray, while the twin positions appear with white and dark contrasts. It can then be clearly seen that the twin migration has produced a displacement of the lower part of the wire of a distance $d_\parallel$ parallel to the twin plane. As a consequence, the wire is deformed by a shear strain also called coupling factor in the shear-coupling grain boundary migration scheme developed in Ref. 20. Since the twin plane is inclined only 6° from the observation direction, the shear strain can be directly given by $\beta = d_\parallel/d_\perp \approx 0.2$. A detailed analysis of this coupling, reported in Ref. 19, shows that the strain produced parallel to the wire axis is of the order of $\varepsilon_p \approx 0.3\%$. This plastic strain can be achieved by the repeated motion of twinning dislocations $\mathbf{b}_{\text{twin}} = (2 - \lambda)^2/(2 + \lambda)^2\ [01\bar{1}\bar{1}]$ with $\lambda = (2/3)^{0.5}\ c/a$ (c and a being the lattice parameters).[21] Interestingly, a moving dislocation (d) above the twin (tw) has been observed. An image difference [Fig. 3(c)] shows that the dislocation has moved in a plane (with a trace tr.P) almost parallel to the wire axis, and thus containing the $\langle c\rangle$ axis. Because the straining axis is also parallel to the wire axis, the resolved shear stress on this dislocation should be very small (the Schmid factor is about 0.1 here). The above observation seems to indicate that the wire surface, covered by an Al/Al_2O_3 layer, plays an important role in the deformation mechanism. In an Al/Al_2Cu eutectic alloy deformed by creep and strained along the lamella axis, dislocations gliding in Al slip planes parallel to the lamella axis were similarly observed.[22] It was attributed to the inhomogeneous deformation between both phases. Similarly, dislocation glide parallel to the wire axis could also occur due to such strain inhomogeneities; it could even take place at the oxide/Be interface. This aspect will be discussed in Sec. V.

In the same wire bundle (the active wire is still delimited in green), Fig. 4 shows the initially flat twin interface along a $(011\bar{2})$ plane slowing down [Fig. 4(a)] and progressively forming a second facet along the $(01\bar{1}\bar{2})$ plane [Figs. 4(b) and 4(c)]. This can be interpreted by the blocking of the twin on the left hand side of the wire which shows a rough surface (Fig. 4) followed by the formation and migration of the second facet. The image difference shown in Fig. 4(d) and corresponding to a time interval of 38 s shows that the facets continue to move, but at a slower speed, around 1 or 2 nm/s. A similar offset on the wire sides indicated by arrows, can be explained by a shear in opposite directions along the two twin planes as sketched in Fig. 4(e). Although difficult to measure, the coupling factor is of the same order of magnitude than previous, which tends to indicate that the same twinning mechanism operates in both facets. This is in agreement with the fact that both facets are conjugate twinning planes.[23] However, because of the shear produced in opposite directions, strain incompatibilities are expected at the twin intersection T [Fig. 4(e)]. This strain is supposed to be released by dislocation emission until the twin stops. Identifying isolated dislocations is difficult, but rapidly changing contrast, typical of dislocation motions, can be evidenced by inspecting the video (see Supplementary Material).

C. Dislocation plasticity

Plastic deformation by dislocation slip near fractured wires has been frequently observed postmortem. Figure 5 shows the fractured end of a wire under different diffraction conditions. It exhibits a ductile profile. The wire axis is here perpendicular to the $\langle c\rangle$ axis. Several shear bands along the prismatic $(1\bar{1}00)$ plane testify about an intense dislocation glide activity. In many cases, dense dislocation tangles involving $\langle a\rangle$ dislocations can be observed. In addition to these shear bands and tangles, two sets of dislocations more widely spaced than in the tangles could be studied in detail, namely dislocations (d_1 and d_2) (Fig. 5). From a contrast analysis in dark field mode using 6 different diffraction vectors, and shown in the Supplementary Material, the Burgers vectors are found to be $\mathbf{b}_{d_1}//\langle c\rangle$ and $\mathbf{b}_{d_2}//[11\bar{2}0]$, i.e., along the $\langle a\rangle$ direction. Additionally, the dislocation habit plane can be determined by using the apparent variation of the dislocation projected length as shown in the Supplementary Material. It was thus found that both d_1 and d_2 dislocations are located in the basal plane. Surprisingly, this result together with the determination of the Burgers vector indicates that dislocations d_1 have a Burgers vector perpendicular to their habit plane, while the dislocations d_2 have a Burgers vector in their habit plane. Whereas dislocations d_1 are supposed to be sessile, dislocations d_2 can glide in their basal plane. Their alignment forming a train of dislocations suggests that they have indeed moved. These dislocations belonging to a plane parallel

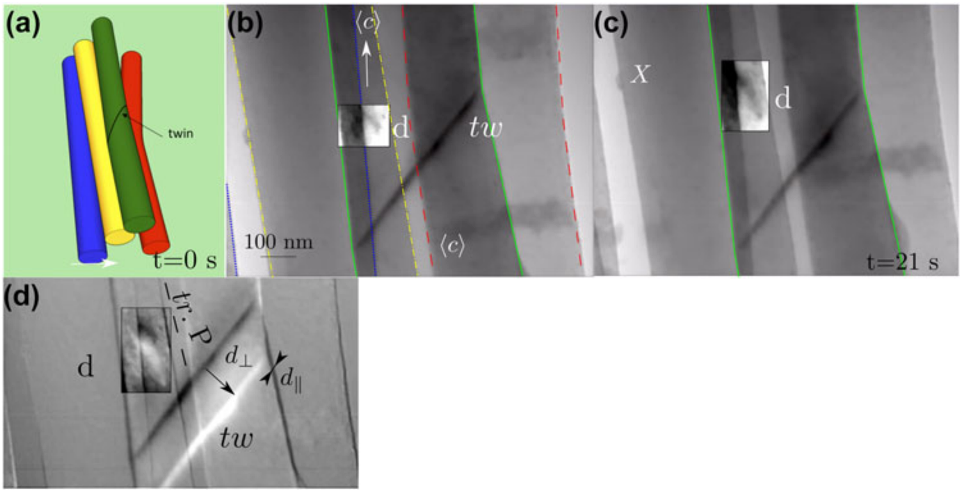

FIG. 3. (a) Sketch of the wires bundle in which only the green one is monitored during the in situ tensile test. The wires are delineated with the same colors in (b). (b)–(c) $(01\bar{1}2)$ $[01\bar{1}\bar{1}]$ twin (tw) motion due to straining. (d) is the image difference (b) − (c). The migration normal to the twin plane ($d_\perp$) leads to a shear displacement parallel to the interface $d_\parallel$. Note the motion of dislocation d in a direction parallel to the wire axis.

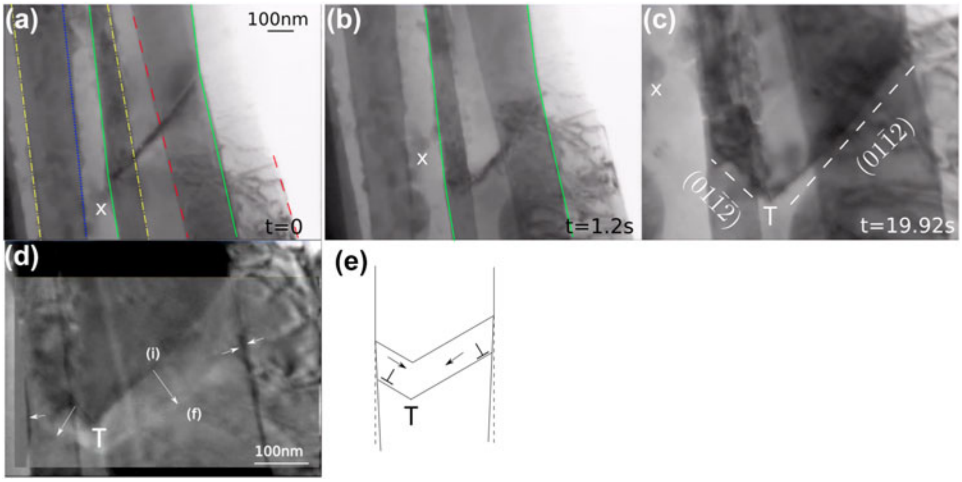

FIG. 4. (a–c) Blocking of the $(01\bar{1}2)$ twin followed by the development of the $(01\bar{1}\bar{2})$ facet. X is a fixed point. (d) shows an image difference highlighting the motion of the facet from an initial position (i) in black contrast to a final position (f) in white contrast. The displacement at the wire side indicates the presence of an associated shear strain represented schematically in (e).

to the wire axis show similarity with the moving dislocation d (Fig. 3). Although dislocations d_2 are glissile, the resolved shear stress in their habit plane is supposed to be very small. Regarding dislocations d_1, they can only move by climb, which appears unlikely in Be at room temperature. As for dislocations d_1, the resolved shear stress acting on d_2 dislocations is supposed to be very low so that climb should operate under osmotic forces.[24] Despite their correlation to plastic deformation, the role of these dislocations in relaxing the applied stress is thus unclear at this point.

Wires oriented along their $\langle c\rangle$ axis are usually brittle but some plastic deformation can be noticed close to the fracture ends. Figure 6 shows a wire end under different diffraction conditions. As observed in Fig. 2, the fractured end appears abrupt and oriented 90° from the wire axis. Few dislocations noted (d_3) can be observed near the end. This highly distorted area prevents a clear analysis of the contrast, but two interesting features can be noted. First, the visibility of some dislocations with a diffraction $\mathbf{g}$ = (0002) indicates that they are not $\langle a\rangle$ type, but presumably $\langle c + a\rangle$ or $\langle c\rangle$ [Fig. 6(a)]. Secondly a $\{10\bar{1}2\}$ twin (tw) can also be observed. As shown in Fig. 3, the twin plane forms an angle of 49° with respect to the wire axis.

Plastic deformation in the observed wires, can be discussed through a Schmid factor analysis. For wires oriented along the $\langle c\rangle$ axis, their Schmid factors for twinning and pyramidal slip with either $\langle c + a\rangle$ or $\langle a\rangle$ dislocations present the highest values, ranging from 0.43 to 0.5, while both basal and prismatic slips exhibit low values, from 0.02 to 0.27. In the orientation where $\langle c\rangle$ is perpendicular to the wire axis, the Schmid factor for prismatic slip becomes important, ranging from 0.43 to 0.49, in the same range than pyramidal slip and twinning, while it is ranging between 0.15 and 0.32 for basal slip. This analysis emphasizes the following features: (i) for wires aligned along the $\langle c\rangle$ axis, the presence of a twin near a fractured end indicates that twinning is indeed the easiest deformation mode (Fig. 3); (ii) for wires whose axis is perpendicular to the $\langle c\rangle$ axis, deformation occurs by shear bands in prismatic plane and involves $\langle a\rangle$ dislocations (Fig. 5). In all cases, basal slip is not geometrically favored although it is the easiest slip system.[16] In bulk samples, because the CRSS of basal slip is about 8 times smaller than for prismatic slip at room temperature,[17] slip systems with low Schmid factor can still be activated. This may explain the presence of $\langle a\rangle$ dislocation moving in the basal plane parallel to the wire axis (d_2 in Fig. 5). Alternatively, the motion of these dislocations may have occurred at the Al/Be interface as discussed below. This could also be the case for dislocations d and d_1. The marginal observation of non-$\langle a\rangle$ dislocations indicates that other slip systems are more difficult to activate. To that respect, the plastic deformation of Be wires does not differ from Be bulk single crystals.[16,17]

IV. DISLOCATION ANALYSIS AT THE Be/Al INTERFACE

Figure 7(a) shows dislocations d_4 separated by about 60 nm in a region located about 4 μm below the moving twin (see Fig. 3), presumably close to the oxide layer. These dislocations are probably interfacial dislocations between the Be and a remaining Al layer below the oxide. To confirm this, we also observed Be wires in regions where the Al matrix was clearly present. Figure 7(b) shows the end of a wire surrounded by the Al matrix. The

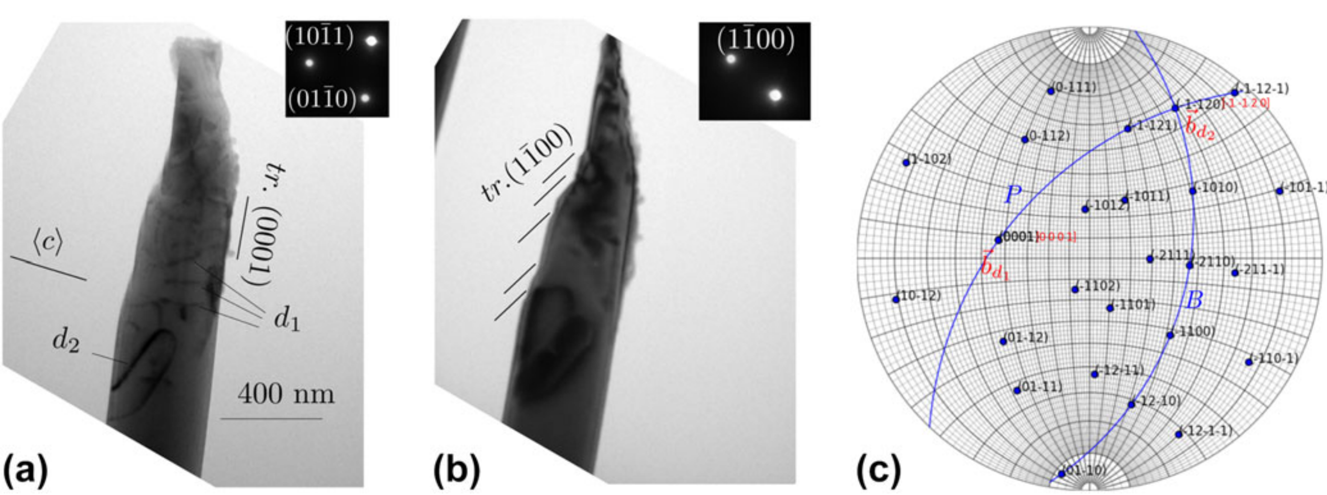

FIG. 5. (a)–(b) Bright field images showing the fractured end of a wire. Steps along the wire indicate an intense dislocation slip along the prismatic plane $(1\bar{1}00)$. Other dislocations noted d_1 and d_2 can be observed. (c) is the stereographic projection of the wire, showing the Burgers vectors, the basal (B) and the $(1\bar{1}00)$ prismatic planes.

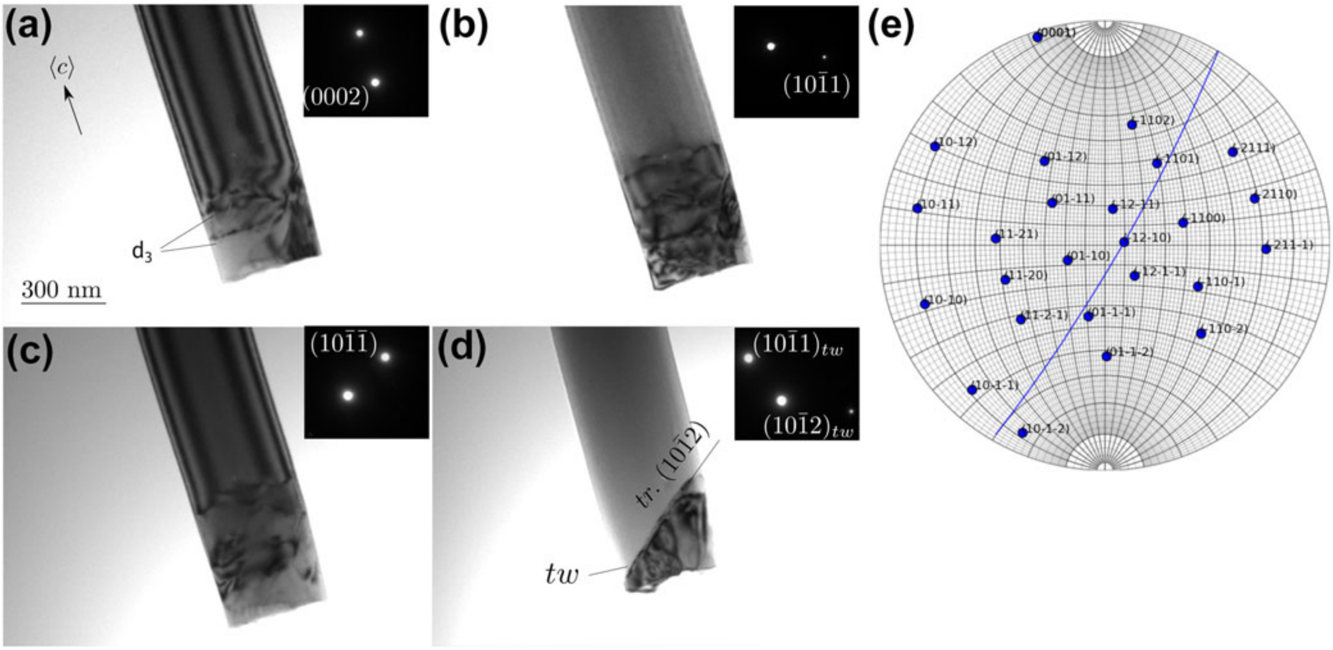

FIG. 6. (a)–(d) Fractured end of a wire under different diffraction conditions (bright field images) showing dislocations (d_3) and twin (tw). (e) is the corresponding stereographic projection where the twin plane is reported.

long axis of the wire corresponds to the ⟨c⟩ axis, the interface planes between Al and Be correspond to two prismatic planes (P_a and P_b). Basal (B) and second order pyramidal planes (π_{2a} and π_{2b}) can also be identified. The orientation relationships Be ($\bar{1}010$)/Al (001) and Be [$1\bar{2}10$]/Al [010] are in agreement with previous studies.[25,26] In the twinned area these relationships become Be (0001)/Al (100) and Be [$1\bar{2}10$]/Al [010]. Interfacial dislocations, noted d_5 in Fig. 7(b), can be observed in P_a. A contrast analysis based on the method described by Ref. 27 was performed for a collection of two beam bright field images taken with 10 diffraction vectors **g**, to determine their Burgers vector. This analysis shown in the Supplementary Material shows that **b** is close to the [001] direction in Al and [$\bar{1}010$] in Be. The Burgers vector is thus normal to the interface plane. Such defect can be produced by decomposition of a lattice dislocation originating from the Be or Al phase into interfacial dislocations. An example of such decomposition is shown on the dichromatic pattern [Fig. 7(c)]. The decomposition products relate lattice sites of each phase. They involve a glissile disconnection with a Burgers vector parallel to the interface and a sessile disconnection with a step character and a Burgers vector close to the normal to the interface, i.e., **b** close to [001] Al/[$10\bar{1}0$] Be. As in the twin area the [001] direction is supposed to be parallel to the [0001] direction in Be [see Fig. 7(c)], the dislocation d_1 identified near the fracture tip in Fig. 5 may also be a dislocation located at the interface between Be and a thin layer of Al left. Its Burgers vector is therefore perpendicular to the plane containing the dislocation lines, which makes it a sessile dislocation. These sessile dislocations can only move by climb, and the fact that they are arranged as a pseudoperiodic array, close to an equilibrium configuration, render their motion even more difficult. Such an accommodation is feasible as discussed in Sec. V.

Interfacial sessile dislocations may also play a role in initiating the nucleation either of perfect lattice dislocations or twinning dislocations in the Be wire. Moreover the observation of a train of dislocations in the basal plane d_2 (Fig. 5), presumably also located at the interface, and moving parallel to the wire axis suggests that they may also play a role in the deformation process. To test this idea, we have performed FEM simulations of a wire surrounded by a thin Al oxide layer.

V. ANALYSIS OF THE STRESS DISTRIBUTION AT THE Al/Be INTERFACE

A. Model description

We consider the geometry of the wire containing a twin as shown in Fig. 3. The model is composed of a cylindrical wire of diameter d = 230 nm and height h_f = 1 μm of Be surrounded by a 15 nm thick alumina layer [Fig. 1(b)]. As a first approximation we considered that the eventual remaining Al layer can be neglected compared to the Al oxide [Fig. 8(a)]. To mimic the possible break of the oxide layer, either during the course of deformation or because of initial imperfections, we choose to remove the oxide along a small strip in the

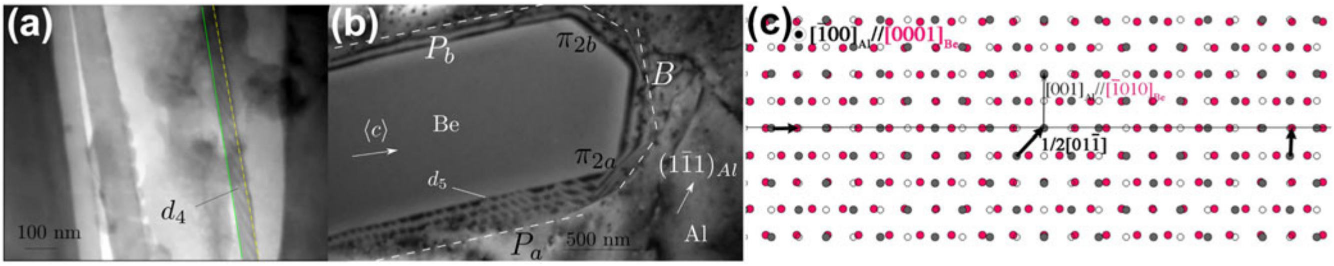

FIG. 7. (a) Dislocations close to the wire surface 4 μm below the twin shown in Fig. 3. (b) End of a Be wire in the Al matrix. (c) Dichromatic pattern showing the decomposition of an Al lattice dislocation at the Be/Al interface. The projection axis is [100] Al//[0001] Be. The interface is underlined in black. The decomposition products consist of a disconnection whose Burgers vector is close to the normal to the interface plane and a glissile dislocation. (Be: Red, Al: Black, open dots correspond to Al lattice sites at $z = 1/2$).

upper part [Fig. 8(a)]. The displacement of the position of the stripped area along the wire leads to similar results. To take into account the elastic anisotropy of the wire, the upper part of the crystal was oriented with the $\langle c \rangle$ axis parallel to the z direction with the corresponding Euler angles (φ_1, Φ, φ_2) = (−158.2, 2.7, −4.8), while the lower part was oriented according to (φ_1, Φ, φ_2) = (134.7, 86.2, 113.7). The Be elastic constants were taken as[28] ($\times 10^{10}$ Pa): $C_{11} = 29.23$, $C_{33} = 33.64$, $C_{44} = 16.25$, $C_{12} = 2.67$, and $C_{13} = 1.4$. The alumina layer is considered to be isotropic with $\rho = 3900$ kg/m^3, $E = 300$ GPa and $\nu = 0.222$. The top surface at $z = h_f$ was displaced along the z direction by 0.005 h_f. The bottom surface was fixed along z while the point (0, 0, 0) along x, y and z directions, and the point (0, d/2, 0) along x and z directions. These conditions prevent the rotation and lateral displacement of the wire during straining. The displacement value was fixed to compare with the typical value of the yield stress, $\sigma_{YS} \approx 1.45$ GPa $\approx 0.005\, E_{Be}$, measured from a micromechanical test on a single wire (Young's modulus of the composite material Be plus oxide is given by the rule of mixture $E_f = fE_{Be} + (1-f)E_{Al_2O_3}$, with f being the volume fraction of the wire. Since $f \approx 0.02$, then $E_f \approx E_{Be}$). FEM calculations were performed using the COMSOL software.

B. Results

We were interested in looking at the deformation produced along the cylinder, to understand why dislocations were observed to move parallel to the z direction, while their Schmid factor being zero. Our initial hypothesis being that of an isotropic cylinder strained uniaxially, we wanted to test more precisely what are the intrinsic Be anisotropy contributions to the strain. To estimate the strain along the wire, we first removed the strain that can be accommodated by slip and twinning in Be, i.e., the strain $\varepsilon_a = 0.005h_f/h_f = 0.005$. The residual strain tensor is then as follows:

$$\bar{\bar{\varepsilon}}_r = \bar{\bar{\varepsilon}} - \begin{pmatrix} 0 & 0 & 0 \\ 0 & 0 & 0 \\ 0 & 0 & \varepsilon_a \end{pmatrix} = \begin{pmatrix} \varepsilon_{xx} & \varepsilon_{xy} & \varepsilon_{xz} \\ \varepsilon_{xy} & \varepsilon_{yy} & \varepsilon_{yz} \\ \varepsilon_{xz} & \varepsilon_{yz} & \varepsilon_{zz} - \varepsilon_a \end{pmatrix} \quad . \tag{1}$$

We then looked at the components of the strain in the plane along the wire, i.e., in the cylinder with a normal $\mathbf{n} = 1/(x^2 + y^2)^{0.5}(x, y, 0)$. Considering that the deformation is accommodated by dislocations in the direction of their Burgers vector $\mathbf{b}$. The residual stress is as follows:

$$\sigma_r = \left(\bar{\bar{\bar{\bar{C}}}}\,\bar{\bar{\varepsilon}}_r \cdot \vec{n}\right) \cdot \vec{b} \tag{2}$$

with C being the stiffness tensor. The stress can be decomposed into radial [$\mathbf{b} = 1/(x^2 + y^2)^{0.5}$ $(x, y, 0)$] (σ_{rr}), tangential [$\mathbf{b} = 1/(x^2 + y^2)^{0.5}$ $(y, -x, 0)$] (σ_{rt}) and longitudinal [$\mathbf{b} = (0, 0, 1)$] (σ_{rl}) components.

The σ_{rr}, σ_{rt} and σ_{rl} components are shown at the interface between Be and the oxide in Figs. 8(b)–8(d) and along the x direction [Figs. 8(f)–8(h)] in the oxide layer at 3 different positions along the wires noted 1, 2 and 3 in Fig. 8(a). While radial and longitudinal components exhibit values larger than few tens of MPa especially at the border of the stripped area, the tangential component is one order of magnitude smaller. At the two borders between the oxide layer and the stripped wire, radial and longitudinal components reach values of the order of 1 GPa [the color scales in Fig. 8(b) and 8(d) have been adjusted between −100 and 100 MPa to highlight stress differences]. Stress profiles in the oxide layer show that the compressive stress decreases and tend to zero at the wire surface for both radial [Fig. 8(f)] and longitudinal [Fig. 8(h)] components. An opposite behavior is found for the tangential component [Fig. 8(g)]. In contrast to the longitudinal component that is substantial only near the twin plane and close to the stripped area, the radial component reaches high values homogeneously along

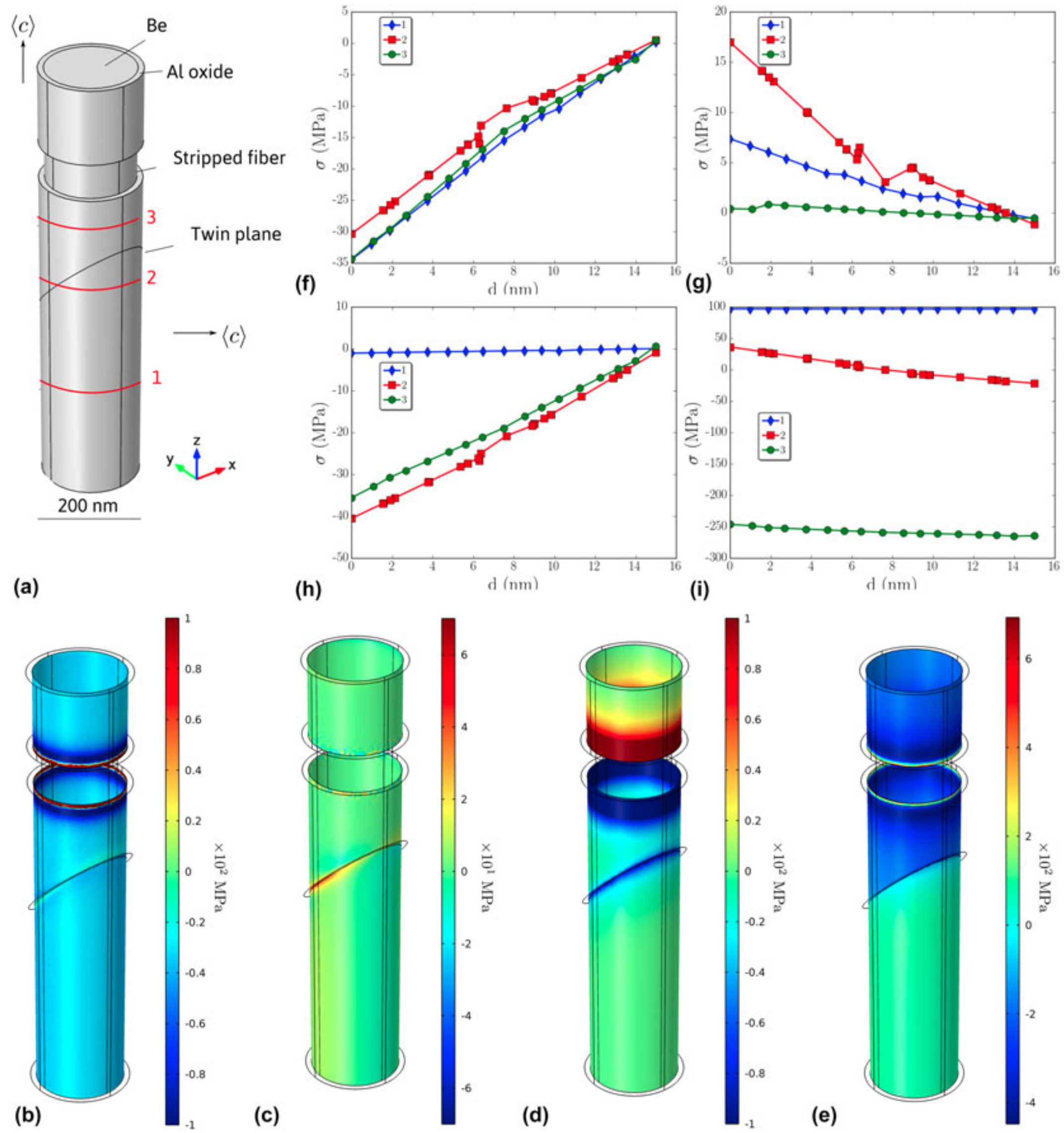

FIG. 8. (a) Description of the model. Radial (b), tangential (c) and longitudinal (d) stress at the interface between the wire and the oxide. (f) to (h) are respectively, radial, tangential and longitudinal stress profiles along the x direction at three different heights [noted 1, 2, 3 in (a)] in the oxide layer (the origin corresponds to the interface location). (e) and (i) correspond to σ_{rz} (see text for details).

the whole wire. This can be qualitatively explained by the large difference of the Poisson ratio between Be (ν_{Be} = 0.032) and Al oxide (ν_{oxide} = 0.222). In first approximation, this difference generates a compressive strain $\varepsilon_{rr} \approx (\nu_{oxide} - \nu_{Be})\varepsilon_a \approx 10^{-3}$. The corresponding stress values obtained are expected to be sufficient to activate dislocation motion at the interface, especially if the oxide layer is locally fractured. The direction of the motion is determined by the force direction, i.e., according to the Peach–Koehler equation:

$$\left(\overline{\overline{\sigma}}_r \cdot \vec{b}\right) \times \vec{u} = \vec{F} \quad , \tag{3}$$

where $\mathbf{u} = 1/(x^2 + y^2)^{0.5}\ (y, -x, 0)$ is the line direction taken tangent to the cylinder. If we consider a Burgers vector $\mathbf{b}$ perpendicular to the interface, i.e., $\mathbf{b} = b/(x^2 + y^2)^{0.5}\ (x, y, 0)$, the components of the force in the radial, tangent and longitudinal directions are $F_r = b\sigma_{rl}$, $F_t = 0$ and $F_l = -b\sigma_{rr}$, respectively. The component of this force is important along the z direction everywhere along the wire as indicated by the σ_{rr} value, and corresponds to a climb force. The glide component is also significant but principally close to the stripped area. However, this force leads to the motion of the dislocation out of the interface in the oxide or Al left layer. If we now consider a Burgers vector $\mathbf{b}$ parallel to the interface, i.e., $\mathbf{b} = b\ (0, 0, 1)$, this yields to the radial, tangent and longitudinal components equal to $F_r = b\sigma_{rz}$, $F_t = 0$ and $F_l = -b\sigma_{rl}$ respectively, where $\sigma_{rz} = C_{13} (\varepsilon_{xx} + \varepsilon_{yy}) + C_{33} (\varepsilon_{zz} - \varepsilon_a)$. In this case, the glide component mainly stands along the z direction, and has also a strong value, especially close to the stripped area. The climb component is radial here and forces the dislocations out of the wire. The stress component σ_{rz} shown in Fig. 8(e), indeed exhibits large compression and tension values. The corresponding stress profile shown in Fig. 8(i) indicates a strong compressive stress (≈250 MPa) above the twin plane and tensile stress (≈100 MPa) below, both almost constant in the oxide layer. These stresses arise because the wire below the twin plane is comparatively softer than the upper part, and deforms more than the upper part for an overall fixed imposed deformation.

In conclusion, we have shown that dislocations with a Burgers vector parallel to the wire (similar to d_2 in Fig. 5) or normal to the Al/Be interface (similar to d_1 in Fig. 5) can take part in plastic relaxation. It is shown that they would nucleate preferentially close to the area where the outer Al oxide is cracked, and where stress concentration arises. This might explain why dislocations d_1 and d_2 were observed close to the fractured area despite having a Schmid factor deduced from the applied longitudinal stress, i.e., close to zero. Because of this remaining oxide, both dislocations experience glide and climb components that are on the order of several tens of MPa. d_2-type dislocations can move by glide along the wire, while d_1-type dislocations are expected to climb along the wire. This latter motion is probably difficult at room temperature due to the necessity of the diffusion process. However, this process cannot be completely ruled out due to (i) a possible easier vacancies/interstitial diffusion along the interface, and (ii) the high stress concentration, especially near the stripped area.

VI. SUMMARY AND CONCLUSIONS

Plastic deformation of submicron Be wires has been investigated by in situ TEM straining experiments. Because Be wires were extracted by electrochemical etching from an eutectic alloy, they stood free of implantation defects such as the ones observed during standard FIB preparation. We showed that the wire deformation behavior is strongly dependent on their orientation due to the strong anisotropy of the hcp structure of Be. To that respect, Be wires tend to behave most similarly to Mg pillars.[11] In dislocation free wires, abrupt fragile-like fracture is recorded presumably associated to a dislocation avalanche triggered at high yield stress. Indeed individual wires tested in SEM show a remarkable high yield stress around 2 GPa.[18] This fragile-like behavior is reinforced by the $\langle c \rangle$ axis orientation of the wire that is unfavorable for the easy prismatic and basal dislocation glide. On the contrary, the twinned area can plastically deform by prismatic slip because its $\langle c \rangle$ axis is almost perpendicular to the wire axis. Twin migration was also observed. This mechanism contributes both to the expansion of the twinned region and to the total plastic deformation. Shear bands along prismatic planes have indeed been observed in twinned regions. Overall, these observations do not reveal abnormal dislocation behavior compared to bulk samples.

However, because most of the wires are initially dislocation free, twins or dislocations have to be nucleated directly from the wire surface and more probably at the Be/Al interface. The role of the interface is revealed by the unusual observation of dislocations with Burgers vectors parallel and perpendicular to the wire axis and lying in planes parallel to the wire. Further investigations indicate that these dislocations are probably dislocations left at the interface between Be and a remaining Al layer, left from the Al matrix of the eutectic alloy, and partially oxidized. FEM analysis of the stress distribution when a composite Be/Al oxide wire is strained uniaxially show that dislocations with both radial and longitudinal Burgers vector participate to strain accommodation. High stress levels can even be reached in the area where the oxide layer is fractured. Contrary to the bulk material, plastic deformation is thus largely dependent on twin/dislocation nucleation processes in the outer shell at the wire surface. The existence of such a shell is hardly inevitable in most metals because of oxidation. As a side effect, the existence of the outer shell may contribute to the blocking of dislocations from emerging at free surfaces, thus leading to strain hardening. This was revealed during the operation of spiral sources in Al naturally oxidized[4] or in purposely coated metallic wires.[29,30] Recent dislocation dynamics simulations performed on various coated pillars deformed in compression tend to confirm the hardening role of the outer shell while preserving the size effect on the yield stress.[31] Unusual plastic accommodation in thin metallic films on substrate has also been evidenced during thermal cycling in Cu. Dislocation glide parallel to the interface has been observed in response to a tensile deformation parallel to the interface. This was interpreted by strain redistribution due to surface and grain boundary diffusion.[32] In conclusion, it appears that modeling pillar or wire mechanical properties would require in the future appropriate descriptions of what was considered in most earlier works as a free surface. This has also been emphasized recently for Pd wires.[33] The importance of diffusional processes occurring preferentially at the interface is thought not only to impact strain accommodation but also probably dislocation/twin nucleation processes. The noncontinuity and heterogeneity of the outer shell, which can arise from the plastic deformation itself, leading to stress concentration, is also a crucial parameter.

ACKNOWLEDGMENTS

The authors would like to thank L. Durand for her assistance in running FEM simulations and D. Lamirault for the sample preparation. This work has been supported by the French National Research Agency under the "Investissement d'Avenir" program reference No. ANR-10-EQPX-38-01.

REFERENCES

1. O. Kraft, P.A. Gruber, R. Mönig, and D. Weygand: Plasticity in confined dimensions. *Annu. Rev. Mater. Res.* **40**, 296 (2010).
2. J.R. Greer and J.T.M. De Hosson: Plasticity in small-sized metallic systems: Intrinsic versus extrinsic size effect. *Prog. Mater. Sci.* **56**, 654 (2011).
3. H. Bei, S. Shim, G. Pharr, and E. George: Effects of pre-strain on the compressive stress–strain response of Mo-alloy single-crystal micropillars. *Acta Mater.* **56**, 4762 (2008).
4. F. Mompiou, M. Legros, A. Sedlmayr, D. Gianola, D. Caillard, and O. Kraft: Source-based strengthening of sub-micrometer Al fibers. *Acta Mater.* **60**, 977 (2012).
5. F. Mompiou and M. Legros: Plasticity mechanisms in sub-micron Al fiber investigated by in situ TEM. *Adv. Eng. Mater.* **14**, 955 (2012).
6. D. Dunstan and A. Bushby: Grain size dependence of the strength of metals: The Hall–Petch effect does not scale as the inverse square root of grain size. *Int. J. Plast.* **53**, 56 (2014).
7. P.S. Phani, K. Johanns, E. George, and G. Pharr: A simple stochastic model for yielding in specimens with limited number of dislocations. *Acta Mater.* **61**, 2489 (2013).
8. J. Sharon, Y. Zhang, F. Mompiou, M. Legros, and K. Hemker: Discerning size effect strengthening in ultrafine-grained Mg thin films. *Scr. Mater.* **75**, 10 (2014).
9. E. Lilleodden: Microcompression study of Mg (0001) single crystal. *Scr. Mater.* **62**, 532 (2010).
10. C.M. Byer, B. Li, B. Cao, and K.T. Ramesh: Microcompression of single-crystal magnesium. *Scr. Mater.* **62**, 536 (2010).
11. C.M. Byer and K. Ramesh: Effects of the initial dislocation density on size effects in single-crystal magnesium. *Acta Mater.* **61**, 3808 (2013).
12. D.M. Norfleet: Sample size effects related to nickel, titanium and nickel-titanium at the micron size scale. Ph.D. thesis, Ohio State University, Columbus, Ohio, 2007.
13. Q. Yu, L. Qi, K. Chen, R.K. Mishra, J. Li, and A.M. Minor: The nanostructured origin of deformation twinning. *Nano Lett.* **12**, 887 (2012).
14. J. Poirier, J. Antolin, and J. Dupouy: Investigations on some deformation modes of beryllium. *Can. J. Phys.* **45**, 1221 (1967).
15. P. Regnier and J.M. Dupouy: Prismatic slip in beryllium and the relative ease of glide in HCP metals. *Phys. Status Solidi* **39**, 79 (1970).
16. J. Beuers, S. Jonsson, and G. Petzow: Tem in situ deformation of beryllium single crystals—A new explanation for the anomalous temperature dependence of the critical resolved shear stress for prismatic slip. *Acta Metall.* **35**, 2277 (1987).
17. A. Couret and D. Caillard: Prismatic slip in beryllium, i. the controlling mechanism at the peak temperature. *Philos. Mag. A* **59**, 783 (1989).
18. F. Mompiou, M. Legros, C. Ensslen, and O. Kraft: In situ TEM study of twin boundary migration in sub-micron Be fibers. *Acta Mater.* **96**, 57 (2015).
19. F. Mompiou and M. Legros: Quantitative grain growth and rotation probed by in situ TEM straining and orientation mapping in small grained Al thin films. *Scr. Mater.* **99**, 5 (2015).
20. J.W. Cahn and J.E. Taylor: A unified approach to motion of grain boundaries, relative tangential translation along grain boundaries, and grain rotation. *Acta Mater.* **52**, 4887 (2004).
21. A. Serra, D. Bacon, and R. Pond: Dislocations in interfaces in the h.c.p. metals—I. Defects formed by absorption of crystal dislocations. *Acta Mater.* **47**, 1425 (1999).
22. M. Ignat, R. Bonnet, D. Caillard, and J. Martin: Creep of lamellar Al–$CuAl_2$ composite. 1. Microstructural observations. *Phys. Status Solidi A* **49**, 675 (1978).
23. J. Christian and S. Mahajan: Deformation twinning. *Prog. Mater. Sci.* **39**, 1 (1995).
24. F. Mompiou and D. Caillard: Dislocation-climb plasticity: Modelling and comparison with the mechanical properties of icosahedral AlPdMn. *Acta Mater.* **56**, 2262 (2008).
25. D.C. Van Aken and H.L. Fraser: The microstructures of rapidly solidified hyper-eutectic AlBe alloys. *Acta Metall.* **33**, 963 (1985).
26. D.C. Van Aken: Crystallographic orientation relationships observed in rapidly solidified Al-Be alloys. In *Dispersion Strengthened Aluminum Alloys*, Y. Kim and W. Griffith, eds. (The Minerals, Metals & Materials Society, Pittsburgh, Pennsylvania, 1988).
27. K. Marukawa and Y. Matsubara: A new method of Burgers vector identification for grain boundary dislocations from electron microscopic images. *Trans. Jpn. Inst. Met.* **20**, 560 (1979).
28. J.F. Smith and C.L. Arbogast: Elastic constants of single crystal beryllium. *J. Appl. Phys.* **31**, 99 (1960).
29. K. Ng and A. Ngan: Effects of trapping dislocations within small crystals on their deformation behavior. *Acta Mater.* **57**, 4902 (2009).
30. S-W. Lee, A.T. Jennings, and J.R. Greer: Emergence of enhanced strengths and Bauschinger effect in conformally passivated copper nanopillars as revealed by dislocation dynamics. *Acta Mater.* **61**, 1872 (2013).
31. J.A. El-Awady, S.I. Rao, C. Woodward, D.M. Dimiduk, and M.D. Uchic: Trapping and escape of dislocations in micro-crystals with external and internal barriers. *Int. J. Plast.* **27**, 372 (2011).
32. T. Balk, G. Dehm, and E. Artz: Parallel glide: Unexpected dislocation motion parallel to the substrate in ultrathin copper films. *Acta Mater.* **51**, 4471 (2003).
33. L.Y. Chen, M. He, J. Shin, G. Richter, and D.S. Gianola: Measuring surface dislocation nucleation in defect-scarce nanostructures. *Nat. Mater.* **14**, 707 (2015).

Supplementary Material

To view supplementary material for this article, please visit https://doi.org/10.1557/jmr.2017.327.

Supplementary Materials

Analysis of dislocations in figure 6

A contrast analysis has been performed on dislocations presented in figure 1a. Both d_1 and d_2 are visible with $\vec{g} = (10\bar{1}3)$ and with $\vec{g} = (\bar{1}01\bar{1})$. Invisibility of the dislocations d_1 with $\vec{g} = (\bar{1}\bar{1}20)$ and its faint residual contrast with $\vec{g} = (\bar{1}010)$, lead to a Burgers vector $\vec{b}_{d_1} \| \langle c \rangle$ direction. Invisibility of the dislocations d_2 with $\vec{g} = (1\bar{1}02)$ and with $\vec{g} = (\bar{1}10\bar{1})$, leads to a Burgers vector $\vec{b}_{d_2} \| [11\bar{2}0]$, i.e. along the $\langle a \rangle$ direction. The Burgers vectors and invisibility conditions are reported in the stereographic projection in Fig. 1b.

The dislocation habit plane can be determined by using the variation of the dislocation apparent width w (Fig. 1c) during a tilt series. The analysis shows that both types of dislocations present the same variation of their apparent width. The normalized width w/w_{max}, with respect to the tilt angle (dots) is reported in figure 1c. The points can be accurately fitted by the full curve representing the theoretical variation of the width of dislocations that are located in the basal plane.

a)

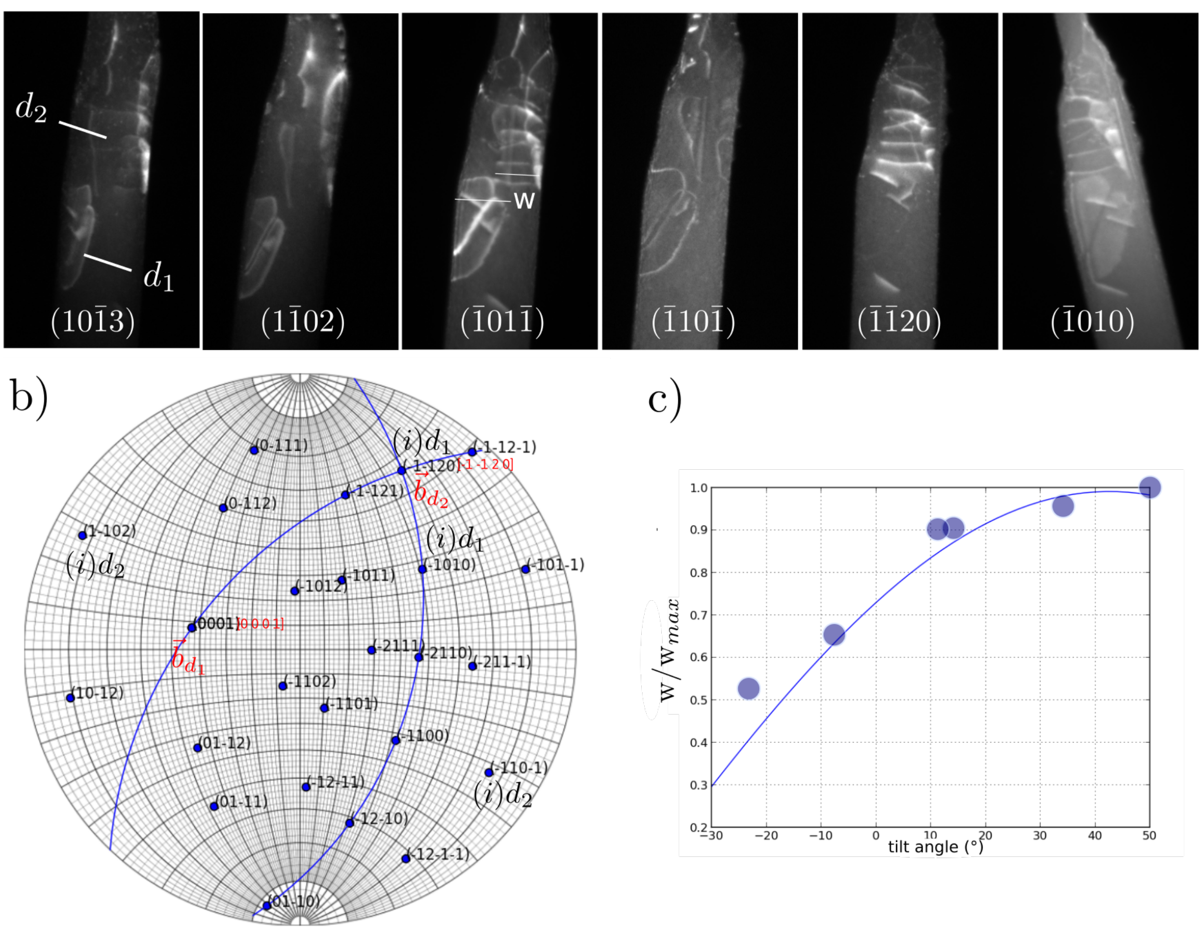

Figure 1: a) Analysis of the contrast of dislocations d_1 and d_2 in dark field mode . b) is the stereographic projection of the wire. c) is the theoretical variation of the apparent dislocation width with the tilt angle in the basal plane and experimental measurements (dots).

Analysis of the interfacial dislocations in figure 8

A contrast analysis, of interfacial dislocations between Al and Be, based on the method described by Marukawa et al. [1], was performed for a collection of two beam bright field images taken with 10 diffraction vectors $\vec{g}$. It is shown in figure 2.

The asymmetric dark(D)/light(L) contrasts at the two sides of the dislocations with respect to the dislocation line oriented from the bottom to the top of the interface indicates that $\vec{g}_i \cdot \vec{b} < 0$ for $i = 1, 3, 4, 8$, $\vec{g}_j \cdot \vec{b} > 0$ for $j = 5, 6, 7$. These conditions restrict the location of the Burgers vector in the colored area in figure 2. Additional faint residual contrasts corresponding to $\vec{g}_k \cdot \vec{b} \approx 0$ are obtained for $k = 2, 9, 10$. This indicates that $\vec{b}$ is close to [001] direction in Al and $[\bar{1}010]$ in Be. The Burgers vector is thus normal to the interface plane.

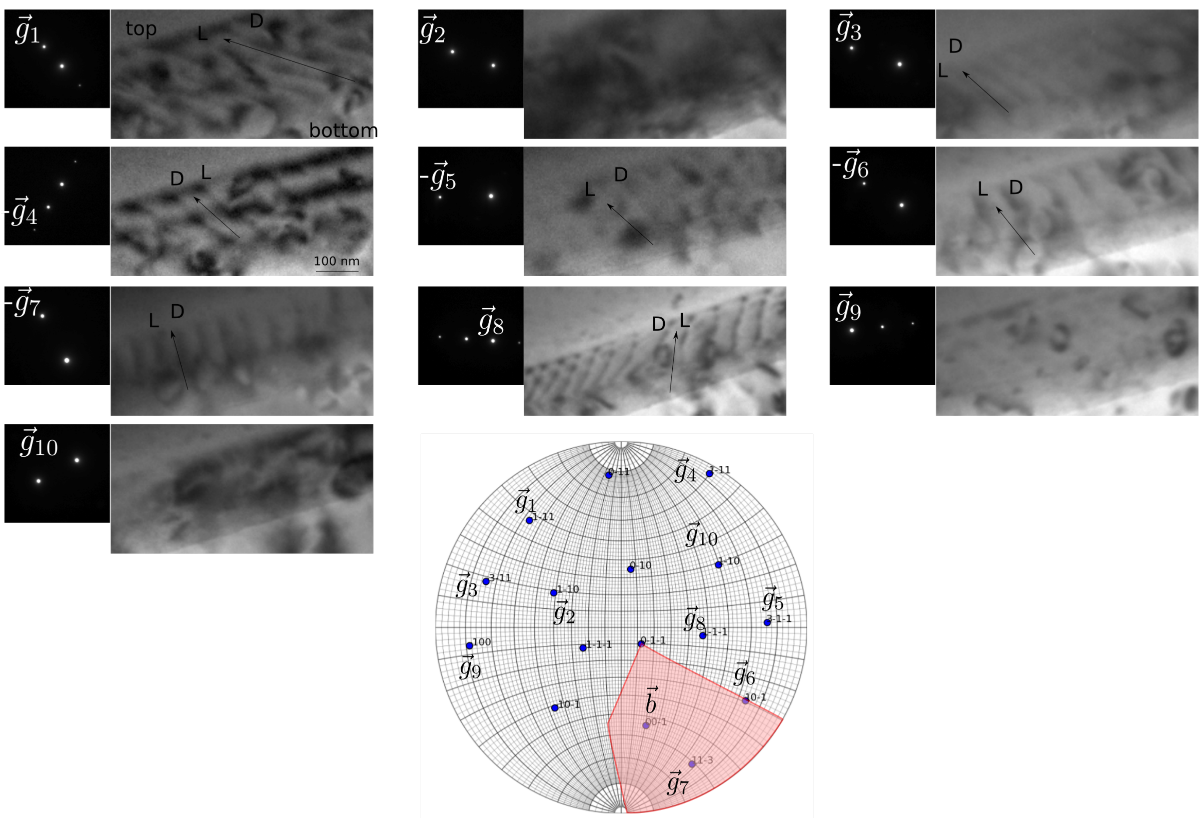

Figure 2: Interfacial dislocation contrast analysis. When $\vec{g} \cdot \vec{b} < 0$ ($\vec{g} \cdot \vec{b} > 0$), the dislocation contrast is asymmetrical with a light (dark) and dark (light) contrast along the line when oriented from the bottom to the top surface. When $\vec{g} \cdot \vec{b} \approx 0$, the dislocation has a faint contrast. The different conditions lead to a Burgers vector located in a colored area in the stereographic projection, presumably close to the [001] direction.

References

[1] K. Marukawa, Y. Matsubara, Trans. Jap. Inst. Metals 20 (1979) 560–568.